nature neuroscience

Sublinear integration underlies binocular processing in primary visual cortex

Fabio Longordo[1], Minh-Son To[1,2], Kaori Ikeda[1] & Greg J Stuart[1]

Although we know much about the capacity of neurons to integrate synaptic inputs *in vitro*, less is known about synaptic integration *in vivo*. Here we address this issue by investigating the integration of inputs from the two eyes in mouse primary visual cortex. We find that binocular inputs to layer 2/3 pyramidal neurons are integrated sublinearly in an amplitude-dependent manner. Sublinear integration was greatest when binocular responses were largest, as occurs at the preferred orientation and binocular disparity, and highest contrast. Using voltage-clamp experiments and modeling, we show that sublinear integration occurs postsynaptically. The extent of sublinear integration cannot be accounted for solely by nonlinear integration of excitatory inputs, even when they are activated closely in space and time, but requires balanced recruitment of inhibition. Finally, we show that sublinear binocular integration acts as a divisive form of gain control, linearizing the output of binocular neurons and enhancing orientation selectivity.

Neurons in the brain typically receive thousands of synaptic inputs, which are integrated in time and space to generate an output signal. As most of these inputs are made on the dendritic tree, research over many years has focused on understanding how the passive and active properties of dendrites influence synaptic integration. A range of forms of synaptic integration have been described, from sublinear, as seen in passive dendrites[1], to supralinear due to generation of dendritic spikes[2–8]. More subtle modifications of synaptic integration have also been described, due to activation of potassium, HCN and persistent sodium channels[9–12]. Evidence for these different forms of synaptic integration is based largely on experiments conducted *in vitro*. Much less is known about how neurons process synaptic inputs while embedded in their network *in vivo*.

The cortex provides an ideal brain region where this issue can be addressed. Single neurons in sensory cortical areas integrate inputs with defined spatial and temporal patterns depending on the characteristics of the stimulus. These early computations are thought to be crucial to the processing of sensory information. While there is emerging evidence that somatosensory stimulation can evoke active forms of dendritic integration *in vivo*[13–16], to what extent this can be generalized across different sensory modalities is unclear. *In vitro* work indicates that supralinear forms of synaptic integration require correlated activity clustered onto the same dendritic location or branch[3,8]. In contrast, when inputs are dispersed onto different branches or activated at different times, linear or sublinear forms of synaptic integration usually occur[8,17–19]. It is only now becoming apparent how synaptic inputs, encoding specific sensory information, are distributed at the dendritic level. Some evidence indicates that sensory information is processed by dendrites in a dispersed manner[20,21], which is less likely to recruit active dendritic processing, whereas other evidence supports clustered activation of synaptic inputs onto the same dendrite[22,23].

Here we examine the integration of synaptic inputs in the binocular region of the primary visual cortex of the mouse *in vivo*. By definition, binocular neurons encode information from the two eyes, providing a model system in which to study how two defined sensory inputs are integrated at the single-cell level. Although extracellular recording has provided a basic understanding of how simple and complex cells integrate binocular information[24,25], this analysis is based exclusively on the firing output of neurons and therefore lacks information on the integration of the underlying synaptic responses. Here we use whole-cell patch-clamp recording *in vivo* to study the synaptic events leading to binocular processing in layer 2/3 pyramidal neurons. We find that small synaptic inputs from the two eyes are integrated linearly, whereas large inputs are integrated sublinearly. Using voltage-clamp and compartmental modeling, we show that sublinear binocular integration cannot be explained solely by nonlinear integration of excitatory inputs but requires balanced recruitment of inhibition. Finally, we find that sublinear integration of binocular synaptic inputs acts as a divisive form of gain control, linearizing the output of binocular neurons and enhancing orientation selectivity.

RESULTS

To investigate the integration of binocular inputs, we made *in vivo* whole-cell current-clamp recordings from layer 2/3 pyramidal neurons in primary visual cortex of anesthetized adult mice. Visual stimuli (sinusoidal drifting gratings) were presented selectively to each eye alone or to both eyes together, by using computer-controlled motorized eye shutters (**Fig. 1a**). To reveal the underlying synaptic response, action potentials were removed using a sliding

[1]Eccles Institute of Neuroscience, John Curtin School of Medical Research, Australian National University, Canberra, Australian Capital Territory, Australia. [2]Department of Human Physiology and Centre for Neuroscience, Flinders University Adelaide, South Australia, Australia. Correspondence should be addressed to F.L. (fabio.longordo@anu.edu.au) or G.J.S. (greg.stuart@anu.edu.au).

Received 21 December 2012; accepted 8 April 2013; published online 5 May 2013; doi:10.1038/nn.3394

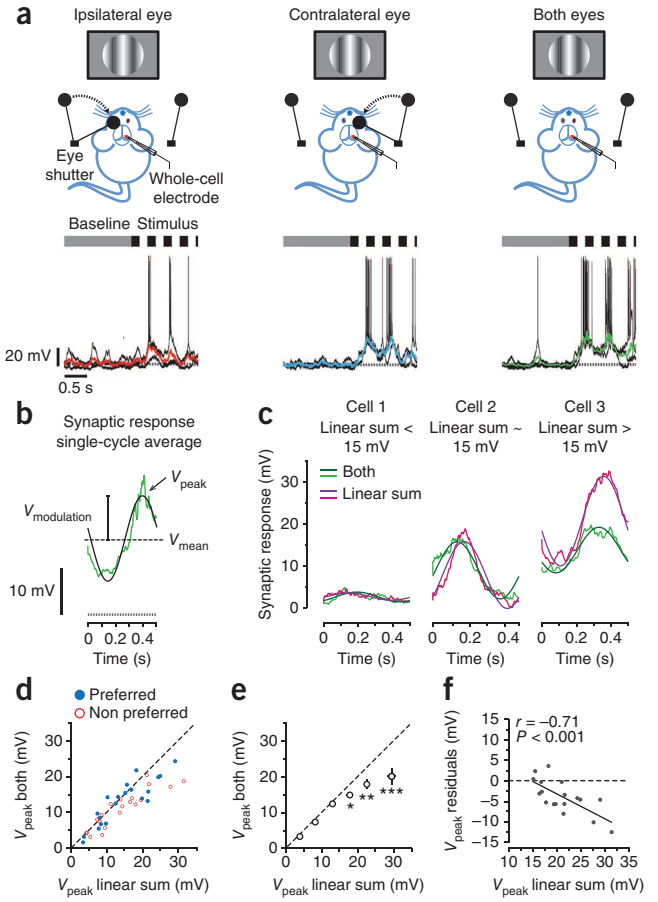

Figure 1 Summation of binocular inputs at the preferred orientation. (**a**) Top: the experimental setup during presentation of the same visual stimulus selectively to each eye alone or to both eyes together, using eye shutters. Bottom: overlaid trials ($n = 3$) of membrane potential during baseline (gray bar, top) and in response to drifting gratings at the preferred orientation (dotted bars, top) during stimulation of the ipsilateral (left) or contralateral eye (middle) and both eyes together (right) with corresponding color-coded median-filtered average responses. Dashed gray line indicates average membrane potential during baseline. (**b**) Single-cycle average of a median-filtered synaptic response (light green) fitted with a sinusoidal function (black). The peak (V_{peak}), mean (V_{mean}) and modulation component ($V_{modulation}$) are indicated. (**c**) Single-cycle synaptic response to stimulation of both eyes (light green) superimposed with the linear sum of contralateral and ipsilateral responses (pink) for three cells with different expected linear sums. Data fitted with sinusoids (dark green and purple). (**d**) V_{peak} of synaptic responses to stimulation of both eyes at the preferred orientation at either the preferred or non-preferred direction versus the corresponding expected linear sum (40 responses, $n = 20$ cells). Dashed diagonal line indicates linear summation. (**e**) Same data as in **d** in 5-mV bins for the expected linear sum and expressed as an average ± s.e.m. ($n = 20$ cells; $^*P < 0.05$, $^{**}P < 0.01$, $^{***}P < 0.001$, two-way ANOVA, Bonferroni post-test). (**f**) Residuals from linearity (difference between observed V_{peak} and expected V_{peak}) versus the expected linear sum. Only residuals for large expected linear sums are shown ($V_{peak} > 15$ mV; 18 responses, $n = 10$ simple cells). Data fitted with a linear regression (black line); r, Pearson's correlation coefficient; P, significance of correlation.

median filter[26] (**Fig. 1a**, bottom). This approach did not appreciably affect the measures we used to characterize subthreshold synaptic responses (**Supplementary Fig. 1**). Median-filtered voltage responses were averaged across trials, as well as over a single cycle of the visual stimulus, fitted with a sinusoidal function and the peak (V_{peak}), mean (V_{mean}), and amplitude of sinusoidal modulation ($V_{modulation}$) quantified (**Fig. 1b**).

Binocular synaptic inputs sum sublinearly

We first restricted our analysis to neurons classified as simple cells (**Supplementary Fig. 2a**,**b**) and focused on synaptic potentials evoked by stimuli at the preferred orientation; that is, the orientation that gave the largest suprathreshold (spiking) response during stimulation of both eyes together. Consistent with earlier work, in adult mice the preferred orientation during stimulation of the ipsilateral or contralateral eye alone was matched in most cells[27] and was similar to that during stimulation of both eyes together (**Supplementary Fig. 2c**). To investigate the integration of synaptic inputs from the two eyes, we compared the synaptic response evoked by stimulation of both eyes together to the linear sum of responses evoked by stimulation of each eye separately. As neurons were poorly direction tuned, with ~85% of cells having a direction selectivity index less than 0.5 (ref. 28) (**Supplementary Fig. 2e**), we pooled responses to the two directions. We found that inputs from the contralateral and ipsilateral eyes added linearly in cells where the expected linear sum was small; however, they added sublinearly in cells where the expected linear sum was large (**Fig. 1c**,**d**). Overall, at the preferred orientation, we observed sublinear integration of binocular synaptic inputs when the peak of the expected linear sum was larger than approximately 15 mV (**Fig. 1e**), with the extent of sublinear integration proportional to the amplitude of the expected linear sum (**Fig. 1f**). Sublinear integration did not depend on the stimulus direction (**Supplementary Fig. 3a**,**b**). We obtained similar results in neurons classified as complex cells (**Supplementary Fig. 4a**–**c**).

We next investigated whether the integration of binocular synaptic responses depends on stimulus orientation (**Fig. 2a**). When averaging across cells, we observed significant sublinear integration only at or near the preferred orientation (**Fig. 2b**). This may arise because responses at the preferred orientation are by definition largest or because the cellular mechanisms generating sublinear integration depend on stimulus orientation. To investigate this, we tested how binocular integration depends on the amplitude of the expected linear sum during stimulation by gratings with different orientations. This analysis showed that, in individual cells, inputs from the two eyes could integrate sublinearly at non-preferred orientations if the expected linear sum was large (**Fig. 2c**,**d**). These data indicate that the orientation dependence of sublinear integration (**Fig. 2b**) arises simply because the proportion of responses with large expected linear sums (>15 mV) is highest at the preferred orientation (**Fig. 2d**; $P < 0.05$, χ^2 test).

Selective presentation of the same visual stimulus to the contralateral or ipsilateral eye alone evoked responses that were often out of phase (**Fig. 2e**). Notably, the extent of sublinear integration was greatest when the phase difference between monocular responses was smallest (**Fig. 2e**,**f**). As seen for stimulus orientation, the phase dependence of binocular integration was due to the higher proportion of responses with large expected linear sums (>15 mV) when monocular responses were in phase (**Fig. 2g**,**h**; $P < 0.01$, χ^2 test). Finally, we investigated the contrast sensitivity of binocular integration. Stimuli were presented at three different contrasts (30%, 50% or 100%; **Supplementary Fig. 3c**). The peak of the synaptic response to stimulation of the contralateral or ipsilateral eye alone increased with increasing contrast (**Supplementary Fig. 3d**), leading to larger expected linear sums at higher contrast. Consistent with an amplitude-dependent

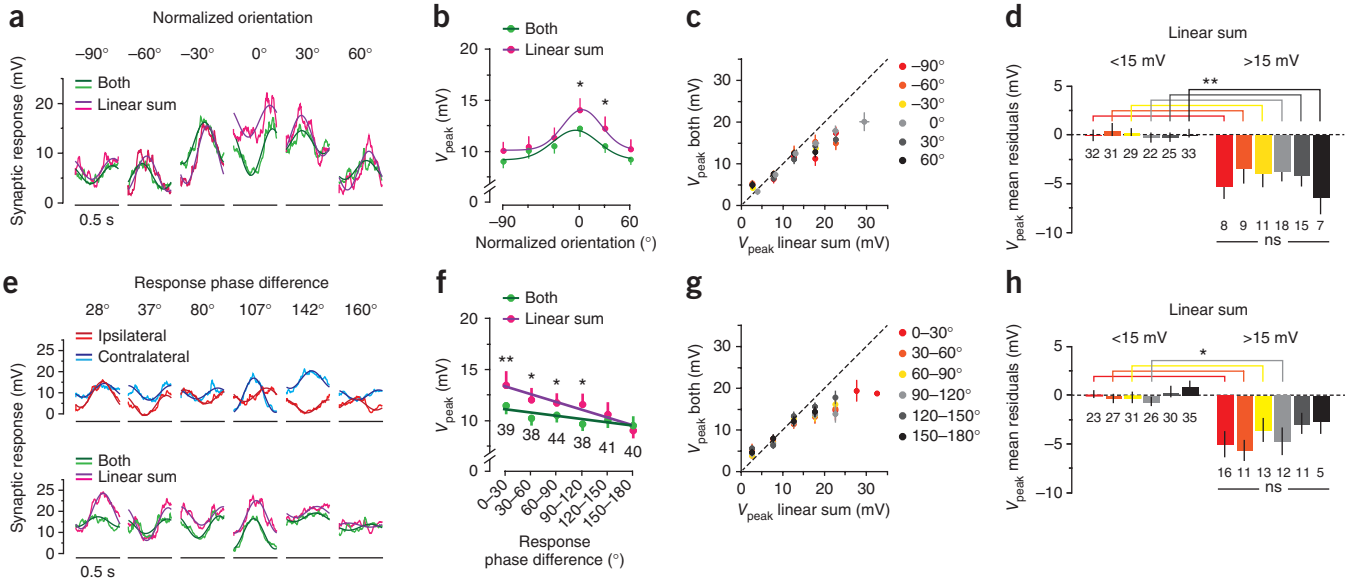

Figure 2 Dependence of binocular integration on stimulus orientation and response phase. (**a**) Single-cycle responses during stimulation of both eyes at six different orientations (light green) together with the corresponding expected linear sum of contralateral and ipsilateral responses (pink). The preferred orientation is 0°. Sinusoidal fits are in dark green and purple. (**b**) Average V_{peak} (± s.e.m.) of responses to stimulation of both eyes together with the expected linear sum plotted as a function of stimulus orientation (40 responses for each stimulus orientation, $n = 20$ cells). Data fitted with a Gaussian. (**c**) Average V_{peak} (± s.e.m.) of responses to stimulation of both eyes color-coded for different stimulus orientations and plotted versus the corresponding expected linear sum in 5-mV bins. Dashed diagonal line indicates linear summation. (**d**) Average residuals from linearity (± s.e.m.) for the different stimulus orientations (same color code as in **c**). Responses sorted based on the amplitude of the expected linear sum. Number of responses in each group indicated below the bars. (**e**) Top: single-cycle responses to stimulation of the contralateral or ipsilateral eye in different cells showing different degrees of phase difference. Bottom: single-cycle responses to stimulation of both eyes together with the expected linear sum for the responses shown in the top. Data fitted with sinusoids. (**f**) Average V_{peak} (± s.e.m.) of responses to stimulation of both eyes together with the expected linear sum plotted as a function of the phase difference between contralateral and ipsilateral responses. Response phase difference binned in 30° bins. Data fitted with a linear regression (number of responses for each phase difference is indicated below the points; $n = 20$ cells). (**g**) Same as **c**, color-coded for phase difference. (**h**) Same as **d**, color-coded for phase difference (same color code as in **g**). Number of responses in each group indicated below the bars. $^*P < 0.05$; $^{**}P < 0.01$; ns, not significant; two-way ANOVA, Bonferroni post-test.

effect, the extent of sublinear integration of binocular responses was greatest at highest contrast (**Supplementary Fig. 3e**,**f**).

One of the main roles of binocular integration is to encode binocular disparity, which is thought to be critical for depth perception. To study how binocular integration depends on the stimulus phase disparity, we made recordings from binocular neurons during presentation of binocular stimuli at six different interocular spatial phase disparities at the preferred orientation using a haploscope (**Fig. 3a**). In these experiments, the initial phase of gratings presented to one eye was fixed while the initial phase of the stimulus to the other eye was systematically varied in 60° increments (**Fig. 3b**). First we presented the stimuli selectively to each eye alone. Changes in the initial phase of the stimulus to one eye led to almost identical changes in the phase of the corresponding monocular synaptic response (**Fig. 3b**,**c**). We then presented the stimuli to both eyes together and studied how binocular synaptic responses integrate as a function of the interocular phase disparity (**Fig. 3d**). At the neuron's preferred phase disparity, defined as the phase disparity that gave the largest suprathreshold (spiking) response (**Fig. 3e**,**f**, top), the phase difference between monocular synaptic responses was smallest (**Fig. 3e**,**f**, bottom) and the extent of sublinear integration was greatest (**Fig. 3g**). This observation, at the single-cell level, is essentially identical to that observed across the cell population when we examined binocular integration of monocular synaptic responses with different phase during presentation of the same visual stimulus to both eyes (see **Fig. 2f**). In summary, these data show that the extent of sublinear integration is greatest at the neuron's preferred phase disparity, when monocular synaptic responses are in phase and binocular responses are of largest amplitude.

Membrane potential responses of simple cells to drifting gratings are commonly characterized by the mean voltage change during the stimulus and by the amplitude of sinusoidal modulation (**Fig. 1b**). Previous work suggests that the cellular mechanisms underlying these components may be different and may encode different aspects of the stimulus[29]. We therefore investigated the integration of these different components during binocular stimulation (**Fig. 4a**). The amplitude of both the mean and modulation components of the binocular response displayed weak orientation tuning (**Fig. 4b**,**c**), with sinusoidal modulation having a higher orientation selectivity index (**Fig. 4d**). To investigate how these different components of the synaptic response integrate during binocular stimulation, we compared the linear sum of each component during stimulation of each eye on its own to the response observed during stimulation of both eyes together (**Fig. 4e**,**f**). Although there was substantial scatter around a line with slope of one (indicating linear integration), when the data were sorted on the basis of peak amplitude we observed sublinear integration of both modulation and mean components when the expected linear sum was large (**Fig. 4g**).

Taken together, these results indicate that sublinear binocular integration is not triggered by a subset of incoming synaptic inputs encoding a specific aspect of the stimulus (for example, preferred versus non-preferred phase disparity). Furthermore, sublinear integration is not restricted to a specific component of the response (mean or modulation).

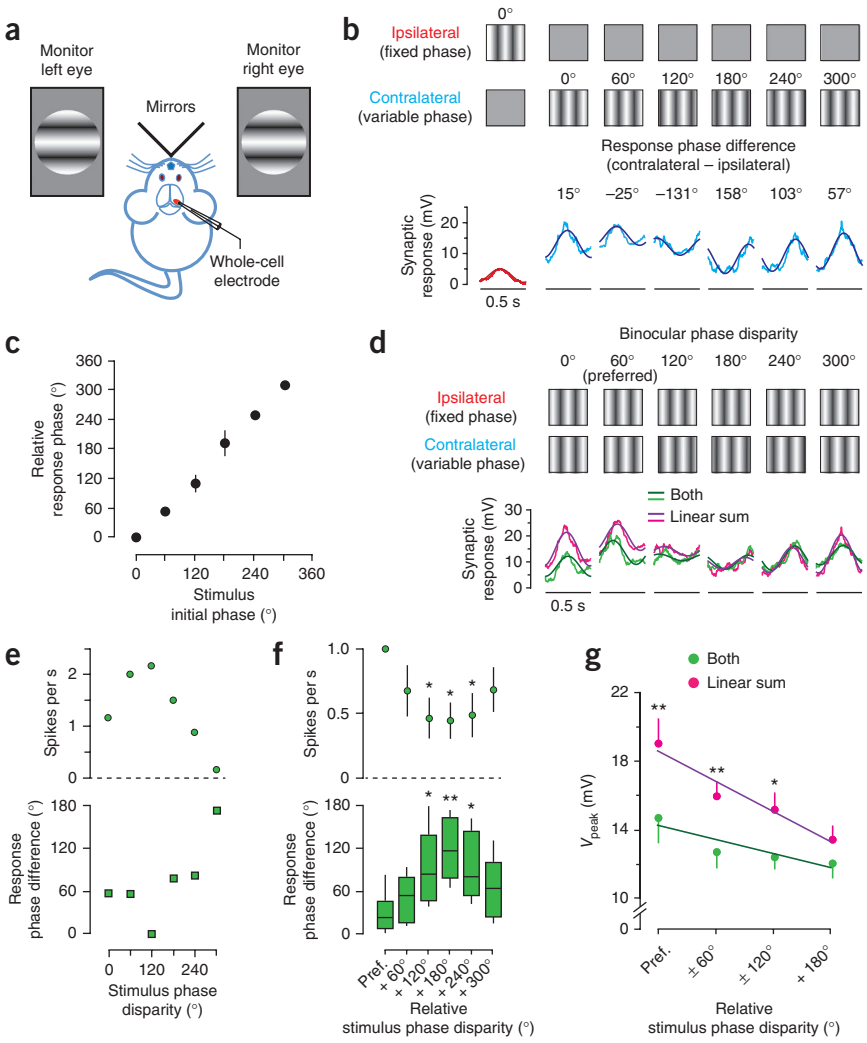

Figure 3 Dependence of binocular integration on phase disparity. (**a**) The experimental setup during presentation of different visual stimuli to each eye with a haploscope. (**b**) Top: monocular stimulation with drifting gratings at the preferred orientation. The initial phase of the stimulus to the ipsilateral eye is kept constant while the initial phase of the stimulus to the contralateral eye is varied. Bottom: single-cycle responses to stimulation of the ipsilateral (red) or contralateral (blue) eye. Data fitted with sinusoids. (**c**) Average relative phase (± s.e.m.) of the monocular synaptic response versus the initial phase of the variable stimulus ($n = 7$ contralateral eye; $n = 4$ ipsilateral eye). In different cells, the monocular response to gratings with initial phase of 0° has been assigned a relative phase of 0°. (**d**) Top: binocular stimuli with different degrees of interocular phase disparity. Bottom: single-cycle responses during stimulation of both eyes at six different interocular phase disparities (light green) together with the corresponding expected linear sum of contralateral and ipsilateral responses (pink). Same cell as in **b**. Sinusoidal fits are shown in dark green and purple. (**e**) Top: spike rate versus stimulus phase disparity for a representative simple cell (preferred phase disparity, 120°). Bottom: phase difference between monocular synaptic responses versus the stimulus phase disparity. (**f**) Top: average spike rates (± s.e.m.) normalized to the response at the preferred phase disparity (Pref.) versus the relative stimulus phase disparity. Bottom: summary of phase difference between monocular synaptic responses versus the relative stimulus phase disparity. Box plots show the median (center bar), interquartile range (box) and range (whisker extent; $n = 7$ cells; $^*P < 0.05$, $^{**}P < 0.01$, one-way ANOVA, Bonferroni post-test). (**g**) Average V_{peak} (± s.e.m.) of responses to stimulation of both eyes and the expected linear sum, plotted as a function of the relative stimulus phase disparity. Responses to 60° and 300° (–60°) stimulus phase disparity or to 120° and 240° (–120°) have been pooled. Data fitted with a linear regression (11 cells; variable stimulus presented to either the contralateral ($n = 7$) or ipsilateral eye ($n = 4$); $^*P < 0.05$, $^{**}P < 0.01$, two-way ANOVA, Bonferroni post-test).

Instead, the extent of sublinear binocular integration depends exclusively on the amplitude of the responses evoked by stimulation of each eye on its own. We therefore conducted a point-by-point analysis of binocular integration in individual cells (**Fig. 4h**). This analysis revealed a strong correlation between the extent of sublinear integration and the amplitude of the expected linear sum during a single visual stimulus (**Fig. 4i**), with an average correlation coefficient of -0.51 ± 0.06 across all cells at the preferred orientation (40 responses, $n = 20$ cells; $P < 0.05$). Applying this point-by-point analysis across all simple cells at all 12 directions produced a stimulus-independent description of the dependence of sublinear binocular integration on the amplitude of the expected linear sum of contralateral and ipsilateral inputs (**Fig. 4j**). Similar results were obtained in complex cells (**Supplementary Fig. 4d**,**e**).

Mechanisms underlying sublinear binocular integration

The observed sublinear integration of binocular synaptic potentials may have a presynaptic origin, due to a reduction in excitation or an increase in inhibition during large responses, or could occur postsynaptically as a result of nonlinear interactions in layer 2/3 pyramidal neurons. To address these possibilities we investigated how excitatory and inhibitory postsynaptic currents (EPSCs and IPSCs) sum during binocular stimulation using somatic whole-cell voltage-clamp recordings. Recordings were made at hyperpolarized (–80 mV; $n = 12$ cells) and depolarized (+20 to +30 mV; $n = 10$ cells) potentials to isolate the excitatory and inhibitory components of the binocular response, respectively[30,31]. EPSCs recorded at the predicted reversal potential for inhibition (–80 mV) during stimulation of both eyes were orientation tuned (**Fig. 5a**,**b**), consistent with previous data in mice during monocular stimulation[30,31]. Notably, EPSCs evoked by stimulation of both eyes together were similar in magnitude to the linear sum of EPSCs evoked during stimulation of each eye alone (**Fig. 5c**). Similarly, IPSCs recorded at depolarized potentials during stimulation of both eyes together were well predicted by the linear sum of IPSCs evoked by stimulation of each eye alone (**Fig. 5d**). These data indicate that inhibitory and excitatory conductance changes sum essentially linearly, arguing against the idea that sublinear integration of voltage responses during binocular stimulation results from reduced excitation or increased inhibition.

We next studied the relationship between excitation and inhibition in single cells during binocular stimulation at the preferred orientation. Excitatory (g_e) and inhibitory (g_i) conductances were estimated

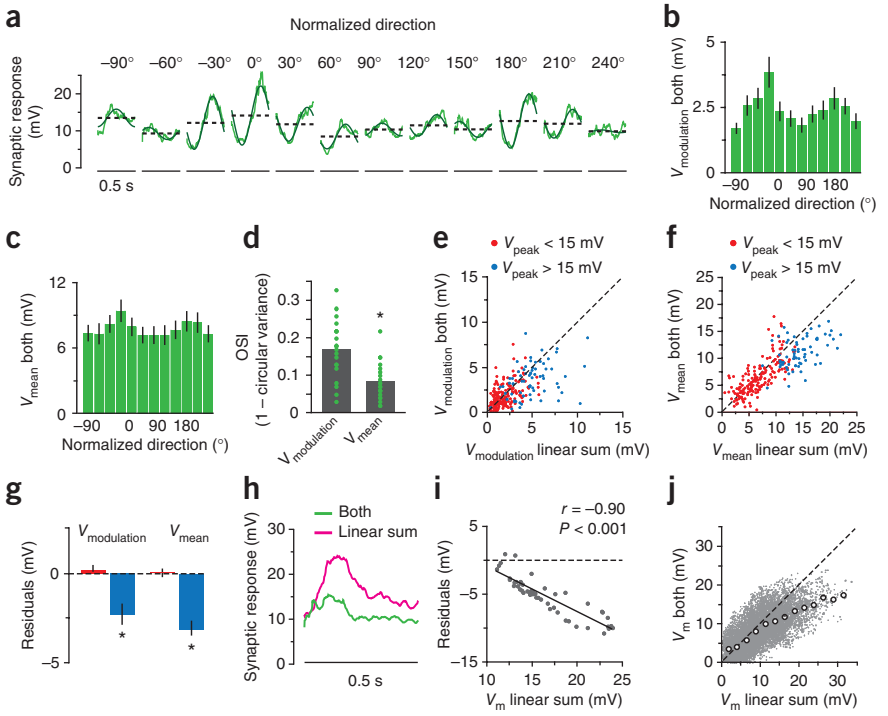

Figure 4 Summation of different components of the synaptic response. (**a**) Single-cycle responses to drifting gratings presented to both eyes at the indicated directions (light green). The preferred direction is indicated as 0°. Data fitted with sinusoidal functions (dark green). Dashed horizontal lines indicate the V_{mean} for each response. (**b**,**c**) Average amplitude (± s.e.m.) of $V_{modulation}$ (**b**) and V_{mean} (**c**) during stimulation of both eyes at 12 different directions (preferred direction defined as 0°; $n = 20$ cells). (**d**) Orientation selectivity index (OSI) of $V_{modulation}$ and V_{mean}. Bars represent mean and points show individual cells ($n = 20$ cells; $^*P < 0.001$, paired t-test). (**e**,**f**) $V_{modulation}$ (**e**) and V_{mean} (**f**) during stimulation of both eyes versus the corresponding expected linear sum (240 responses to 12 stimulus directions, $n = 20$ cells). V_{peak} linear sum < 15 mV, $n = 172$ responses; V_{peak} linear sum > 15 mV, $n = 68$ responses. Dashed diagonal line indicates linear summation. (**g**) Average residuals from linearity (± s.e.m.) for $V_{modulation}$ and V_{mean} for small (red) and large (blue) expected linear sums ($n = 20$ cells; $^*P < 0.001$, two-way ANOVA, Bonferroni post-test). (**h**) Representative observed (both) and predicted (linear sum) synaptic responses used for point-by-point analysis of sublinear integration during a single response. (**i**) Residuals from linearity versus the expected linear sum for the response shown in **h** after binning in 10-ms epochs. Data were fitted with a linear regression (black line); r, Pearson's correlation coefficient; P, significance of correlation. Compare with **Figure 1f**. (**j**) Pooled data during stimulation of both eyes together. V_m binned in 10-ms epochs; 12,000 time bins from 240 averaged responses to 12 stimulus directions in 20 simple cells. Small gray symbols indicate individual data points. Large open symbols indicate average ± s.e.m. after binning in 2.5 mV increments. Dashed diagonal line indicates linear summation.

using previously published methods[32,33]. This analysis revealed that g_e and g_i in individual neurons increased in a proportional manner during stimulation of both eyes together (**Fig. 5e**; average correlation = 0.95 ± 0.01, $n = 9$ cells; $P < 0.01$). The ratio of inhibition to excitation (g_i/g_e), estimated from the slope of linear fits to data from individual cells, indicated that inhibition and excitation were recruited in a balanced manner, with an average ratio close to 1 (1.12 ± 0.18; $n = 9$).

Consistent with this analysis, the average reversal potential of evoked synaptic currents during binocular stimulation was approximately halfway between the predicted reversal potential for excitation and inhibition (–45.8 ± 3.7 mV; $n = 9$). These data indicate that excitation and inhibition are recruited in a balanced manner during binocular visual input.

That EPSCs and IPSCs sum essentially linearly during binocular stimulation suggests that sublinear integration of binocular synaptic potentials has a postsynaptic origin. To investigate this further, we simulated visual responses in a morphologically realistic model of a layer 2/3 pyramidal neuron in which contralateral and ipsilateral excitatory and inhibitory inputs were recruited linearly in a balanced

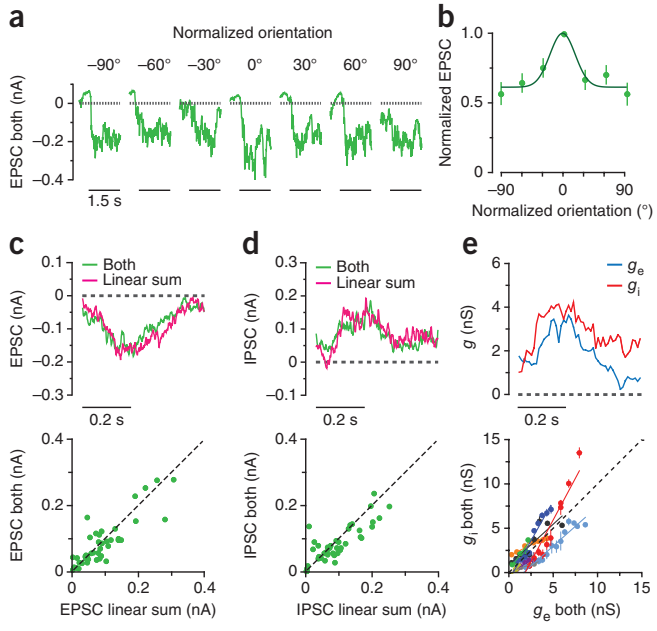

Figure 5 Recruitment and summation of excitation and inhibition during binocular integration. (**a**) EPSCs recorded at –80 mV in response to stimulation of both eyes with drifting gratings at six different orientations. (**b**) Normalized EPSC amplitude (± s.e.m.; averaged over the duration of the stimulus) during stimulation of both eyes versus stimulus orientation (preferred orientation defined as 0°; $n = 12$ cells). Data fitted with a Gaussian. (**c**,**d**) Top: single-cycle EPSC (**c**; recorded at –80 mV) and IPSC (**d**; recorded at +20 mV) in response to stimulation of both eyes at the preferred orientation together with the linear sum of EPSCs (**c**) and IPSCs (**d**) evoked by stimulation of each eye alone. Bottom: peak EPSC (**c**; $n = 44$ responses, $n = 11$ cells) and IPSC (**d**; $n = 40$ responses, $n = 10$ cells) amplitude evoked by stimulation of both eyes with gratings at four different orientations (preferred, +30°, +60°, +90°) versus the corresponding linear sum. (**e**) Top: single-cycle average of estimated excitatory (g_e) and inhibitory (g_i) conductance changes in a single cell in response to gratings at the preferred orientation. Bottom: g_i versus g_e ($n = 9$ cells). Data from individual cells (represented by different colors) binned at 0.5-nS increments for g_e and expressed as average ± s.e.m. Colored lines represent linear fits to each data set.

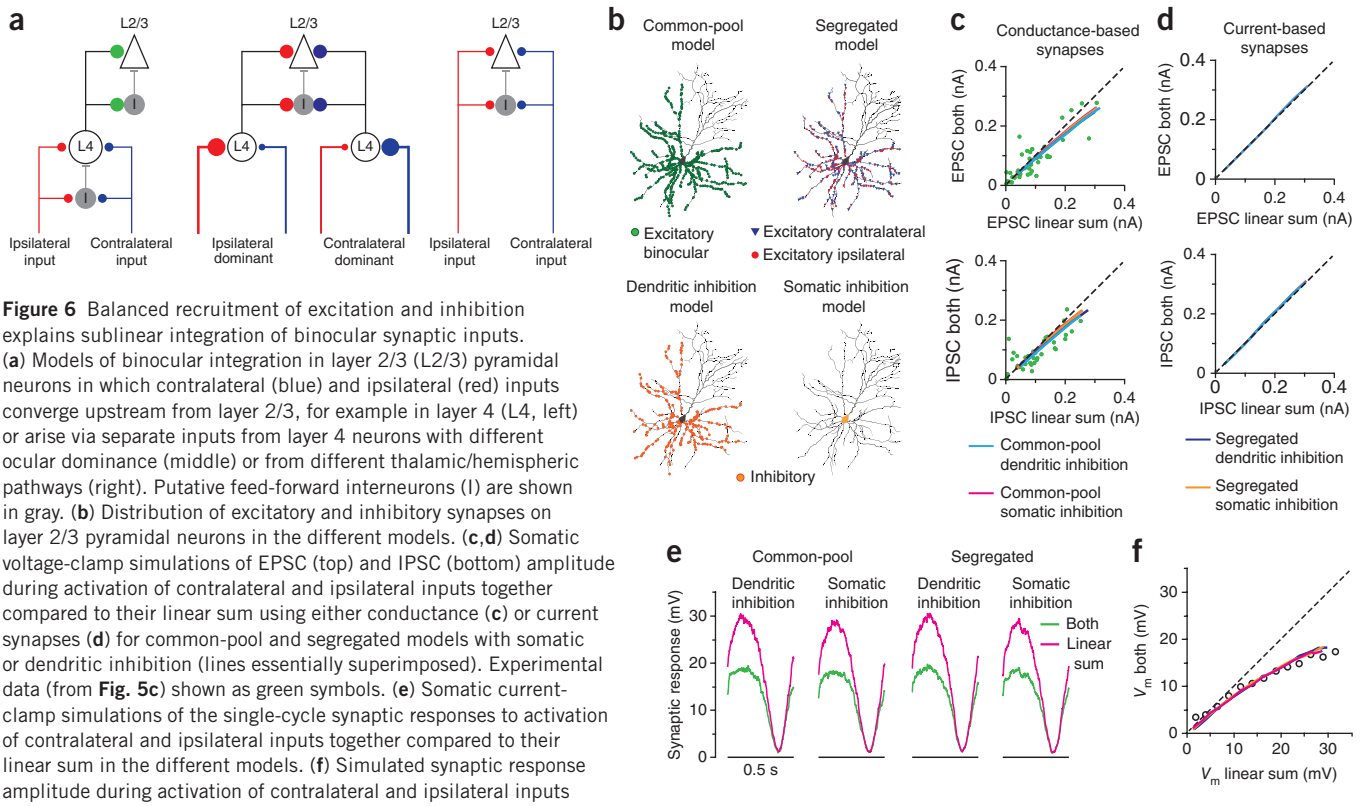

Figure 6 Balanced recruitment of excitation and inhibition explains sublinear integration of binocular synaptic inputs. (**a**) Models of binocular integration in layer 2/3 (L2/3) pyramidal neurons in which contralateral (blue) and ipsilateral (red) inputs converge upstream from layer 2/3, for example in layer 4 (L4, left) or arise via separate inputs from layer 4 neurons with different ocular dominance (middle) or from different thalamic/hemispheric pathways (right). Putative feed-forward interneurons (I) are shown in gray. (**b**) Distribution of excitatory and inhibitory synapses on layer 2/3 pyramidal neurons in the different models. (**c**,**d**) Somatic voltage-clamp simulations of EPSC (top) and IPSC (bottom) amplitude during activation of contralateral and ipsilateral inputs together compared to their linear sum using either conductance (**c**) or current synapses (**d**) for common-pool and segregated models with somatic or dendritic inhibition (lines essentially superimposed). Experimental data (from **Fig. 5c**) shown as green symbols. (**e**) Somatic current-clamp simulations of the single-cycle synaptic responses to activation of contralateral and ipsilateral inputs together compared to their linear sum in the different models. (**f**) Simulated synaptic response amplitude during activation of contralateral and ipsilateral inputs together plotted versus the linear sum for the different models (lines essentially superimposed; same color code as in **c**). Experimental data (from **Fig. 4j**) shown as open symbols.

manner, to match our experimental observations (**Fig. 5e**). We modeled two scenarios. In one scenario, contralateral and ipsilateral inputs converged upstream from layer 2/3, for example in layer 4 (**Fig. 6a**, left). In the second scenario, separate contralateral and ipsilateral inputs converged onto layer 2/3, either from layer 4 neurons with different ocular dominance (**Fig. 6a**, middle)[34] or through different thalamic or hemispheric pathways (**Fig. 6a**, right)[35]. To simulate these two scenarios, we sampled ipsilateral and contralateral excitatory inputs either from a common pool or from two segregated pools of synapses distributed randomly onto basal dendrites (**Fig. 6b**, top). Inhibitory inputs were distributed randomly onto basal dendrites or placed at the soma (**Fig. 6b**, bottom). We simulated our voltage-clamp data (**Fig. 5**) using a realistic value of the somatic series resistance (35 MΩ) and adjusted the resting membrane properties of the model to match the average holding currents recorded at hyperpolarized and depolarized potentials. Excitatory and inhibitory inputs were randomly activated by means of sinusoidally modulated independent Poisson processes in a balanced manner so that the magnitude and ratio of inhibitory to excitatory synaptic conductances estimated from somatic voltage-clamp simulations was similar to that observed experimentally (**Supplementary Fig. 5**; compare with **Fig. 5e**). As one would expect owing to space-clamp errors associated with voltage-clamping neurons with complex dendritic trees[36], the real excitatory and inhibitory conductances required to match the experimental data were substantially larger than that estimated from somatic voltage-clamp, particularly in models with dendritic inhibition (**Supplementary Fig. 5**). Furthermore, proportionally more inhibition was required to simulate the experimentally recorded inhibitory-to-excitatory conductance ratio (g_i/g_e = 1.12) in models with dendritic inhibition, whereas the opposite situation was observed in models with somatic inhibition (**Supplementary Fig. 5**). These simulations highlight issues with the interpretation of excitatory and inhibitory conductance estimates from somatic voltage-clamp data in neurons with dendrites.

Linear recruitment of ipsilateral and contralateral excitatory inputs, separately or together in a balanced manner with inhibition, generated excitatory and inhibitory currents that summed in a manner similar to that observed experimentally (**Fig. 6c**). Essentially no difference in voltage-clamp responses at the soma was observed in models with common compared to segregated ipsilateral and contralateral excitatory inputs (**Fig. 6c**). These simulations predicted a small amount of sublinear summation of excitatory and inhibitory currents during large responses, which was absent in models with current-based synapses (**Fig. 6d**), indicating that it results from poor voltage or space clamp. The capacity of this linear recruitment model to accurately predict our voltage-clamp data further substantiates our conclusion that sublinear integration of voltage responses arises postsynaptically and is not due to a decrease in excitatory drive or an increase in inhibitory drive during large binocular responses.

We next used these models to simulate voltage responses at the soma during stimulation of contralateral and ipsilateral inputs alone or together. In these simulations we adjusted the passive properties of the model to match those observed experimentally at the resting membrane potential during current-clamp recordings. These simulations accurately predicted the extent of sublinear integration of voltage responses observed experimentally during binocular stimulation (**Fig. 6e**,**f**). Notably, we were not able to distinguish between models with common or segregated ipsilateral and contralateral input, indicating either model is valid. Furthermore, we could not distinguish between models with somatic or dendritic inhibition.

As the extent of sublinear summation depends on the relative location of synaptic inputs, we generated additional models with different

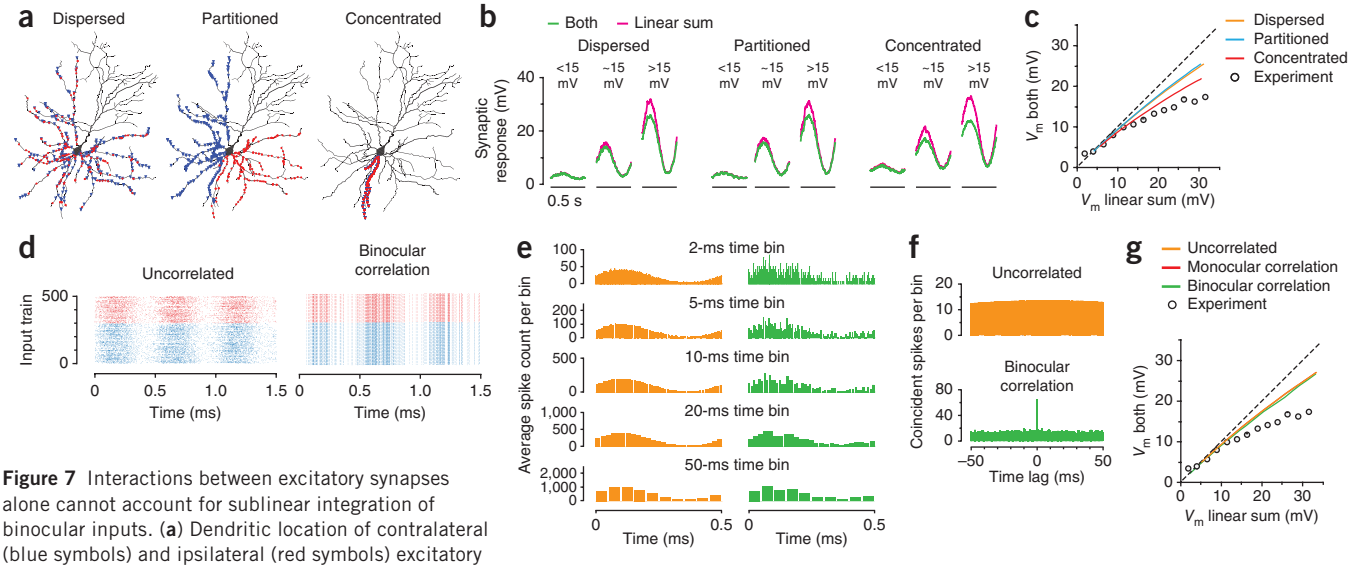

Figure 7 Interactions between excitatory synapses alone cannot account for sublinear integration of binocular inputs. (**a**) Dendritic location of contralateral (blue symbols) and ipsilateral (red symbols) excitatory synapses on the basal dendrites of the layer 2/3 pyramidal neuron model. Synapses were distributed in three different spatial configurations. (**b**) Somatic current-clamp simulations of synaptic responses during activation of contralateral and ipsilateral inputs together at different intensities to evoke responses of different amplitude (linear sum <15 mV, ~15 mV and >15 mV) for the different configurations. Corresponding expected linear sums are superimposed. (**c**) Simulated synaptic response amplitude during activation of contralateral and ipsilateral inputs together plotted versus the linear sum for the different models together with experimental data (open symbols, from **Fig. 4j**). (**d**) Raster plots of uncorrelated (left) and correlated (right) spike trains driving contralateral (blue) and ipsilateral (red) sets of synapses during binocular stimulation. Correlations were introduced by using common Poisson trains to drive sets of 50 synapses. (**e**) Peristimulus time histograms (PSTHs) of the spike trains shown in **d** averaged over six stimulation cycles for the indicated time windows for uncorrelated (left) and binocularly correlated (right) inputs. (**f**) Cross-correlogram (1-ms bins) averaged across all pairs of input spike trains for uncorrelated and binocularly correlated spike trains. (**g**) Simulated synaptic response amplitude during activation of contralateral and ipsilateral sets of inputs in the dispersed model versus the corresponding expected linear sums for the uncorrelated, monocularly correlated and binocularly correlated models, together with the experimental data (open symbols, from **Fig. 4j**). Orange, red and green lines are essentially superimposed.

spatial distributions of excitatory input: either dispersed randomly throughout the entire basal dendritic tree, partitioned into different basal dendritic regions or concentrated onto a single dendritic branch (**Fig. 7a**). We omitted inhibition in these models to determine the extent with which nonlinear interactions between ipsilateral and contralateral excitatory inputs alone contributes to sublinear integration of binocular inputs. As observed experimentally, small contralateral and ipsilateral responses summed linearly, whereas larger responses summed sublinearly (**Fig. 7b**,**c**). The extent of sublinear binocular integration was greatest when contralateral and ipsilateral synapses were concentrated onto a single dendritic branch; however, even in this extreme case, sublinear integration was substantially less than that observed experimentally (**Fig. 7c**).

Finally, we tested the impact of temporal correlations between excitatory inputs. Temporal correlations were made either within (monocular correlation) or between (binocular correlation) contralateral and ipsilateral inputs by using the same Poisson input train to drive multiple sets of synapses in the dispersed model (**Fig. 7d**). We characterized the extent of these correlations by comparing the number of activated excitatory inputs in different time windows (**Fig. 7e**). As expected, the introduction of temporal correlations increased the proportion of synapses that were simultaneously activated; however, the difference between uncorrelated and correlated models rapidly decayed when we considered correlations over longer time windows, still relevant for nonlinear interactions (**Fig. 7e**,**f**). As a result, introduction of temporal correlations either within or between contralateral and ipsilateral inputs did not appreciably affect the degree of sublinear integration of excitatory inputs (**Fig. 7g**). Together, these simulations reveal that nonlinear interactions between excitatory inputs alone are not sufficient to explain the extent of sublinear binocular integration observed experimentally, emphasizing the importance of balanced recruitment of inhibition.

Impact of sublinear integration on action potential output

What is the impact of sublinear binocular integration on action potential output? To address this issue, we first described the relationship between the underlying membrane potential and action potential output in individual cells using a previous model[19] (**Fig. 8a**). Using this model, we could accurately predict, on the basis of median-filtered voltage responses in single cells, the firing rate observed experimentally, confirming the model's validity (**Fig. 8b**). We then used this model to predict action potential output assuming linear summation of synaptic responses and compared the predicted firing rate to that observed experimentally (**Fig. 8c**,**d**). As expected from the highly nonlinear relationship between membrane potential and action potential output (**Fig. 8a**), firing rates observed during stimulation of both eyes together were substantially lower than those predicted by the linear sum of synaptic potentials during stimulation of each eye separately (**Fig. 8d**). Furthermore, when we plotted the observed and predicted firing rates against the linear sum of monocular responses, these data indicated that sublinear integration of binocular responses significantly reduces the gain of the binocular input/output relationship (**Fig. 8e**). This reduction in gain acts to 'linearize' the output of binocular cells, such that the firing rate during binocular stimulation is equal to the linear sum of the firing rates during stimulation of each eye on its own (**Fig. 8f**; linear fit to the observed spike rates: slope = 1.02 ± 0.06, $r^2 = 0.6$, $P < 0.001$). We observed a similar impact of sublinear binocular integration on the gain of the binocular input/output relationship in complex cells (**Supplementary Fig. 4f**).

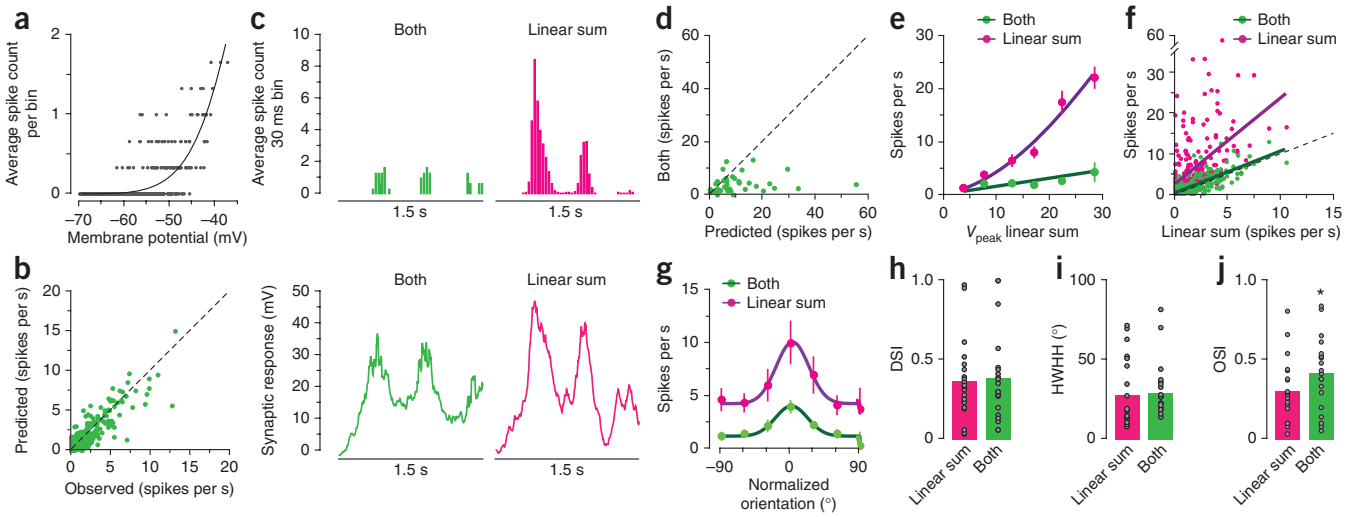

Figure 8 Impact of sublinear binocular integration on action potential output. (**a**) Average spike count versus membrane potential (30-ms bins) for one cell. Data fitted with a threshold nonlinearity model (black trace; $k = 1.16 \times 10^{-5}$, $p = 4.46$; ref. 19). (**b**) Average spike rates predicted using the threshold nonlinearity model during stimulation of both eyes together versus the experimentally observed spike rates (240 responses to 12 stimulus directions, $n = 20$ cells). Spike rate calculated over the 1.5 s period of stimulus presentation. The dashed diagonal line indicates a perfect correlation between predicted and observed values. (**c**) PSTHs of observed action potential output during stimulation of both eyes together at the preferred orientation (top left, 30-ms bins) and corresponding synaptic response (bottom left), together with the predicted action potential output (top right, 30-ms bins) for the same cell assuming linear sum of contralateral and ipsilateral synaptic responses (bottom right). (**d**) Pooled data of the observed spike rate during stimulation of both eyes together plotted versus the predicted spike rate assuming linear summation of synaptic responses to each eye alone (40 responses to preferred stimuli, $n = 20$ cells). (**e**) Summary of observed (green symbols) and predicted (pink symbols) spike rates (± s.e.m.) as a function of the expected linear sum of V_{peak} (in 5 mV bins). Data fitted with the same function as used in **a** to describe the relationship between membrane potential and spike output. (**f**) Summary of observed (green symbols) and predicted (pink symbols) spike rates as a function of the linear sum of the spike rates evoked by stimulation of each eye separately. Data fitted with a linear function (slope = 1.02 ± 0.06 for observed spike rates, dark green line; slope = 2.12 ± 0.24 for predicted spike rates, purple line; $P < 0.0001$). Dashed diagonal line indicates linear summation of spike rate. (**g**) Average tuning curves based on the observed (green) and predicted (pink) spike rates (± s.e.m.) during presentation of gratings at different orientations to both eyes. Data fitted with a Gaussian. (**h–j**) Direction selectivity index (DSI, **h**), tuning width (HWHH, half width at half height; **i**) and orientation selectivity index (OSI, **j**) observed during stimulation of both eyes (green) together with that predicted assuming linear summation of ipsilateral and contralateral inputs (pink). Bars represent means and points show individual cells ($n = 20$ simple cells; $^*P < 0.05$, paired t-test).

We next characterized the impact of sublinear integration on the tuning properties of individual neurons during stimulation with drifting gratings. Consistent with a divisive transformation of the input/output relationship, firing rates were reduced significantly more at the preferred compared to the orthogonal orientation (**Fig. 8g**; orthogonal reduction, 3.47 ± 0.97 spikes per second; preferred reduction, 6.81 ± 1.95 spikes per second; $n = 20$; $P < 0.05$, paired t-test). Analysis of tuning properties based on observed and predicted firing rates showed that, on average, sublinear binocular integration of synaptic responses did not alter direction selectivity (**Fig. 8h**) or tuning half width (**Fig. 8i**), but enhanced orientation selectivity (**Fig. 8j**). A similar impact of sublinear integration on orientation selectivity was observed in a subset of cells with 'in-phase' monocular responses at the preferred orientation (**Supplementary Fig. 6**), indicating that this is not due to a complex interaction between stimulus orientation and the relative phase of contralateral and ipsilateral responses.

DISCUSSION

Here we describe the integration of binocular synaptic inputs in layer 2/3 pyramidal neurons from mouse primary visual cortex. The main finding is that small inputs from the two eyes are integrated linearly, whereas large inputs are integrated sublinearly. Sublinear integration depends solely on the amplitude of the incoming inputs and is not restricted to information encoding particular aspects of the visual stimulus, such as orientation, direction, contrast or binocular phase disparity. Furthermore, sublinear binocular integration is not a result of network interactions upstream from layer 2/3 pyramidal neurons but occurs postsynaptically owing to nonlinear interactions between excitatory and inhibitory inputs recruited in a balanced manner. This amplitude-dependent sublinear integration reduces the gain of the input/output relationship of binocular neurons, linearizing action potential output and increasing orientation selectivity.

Previous work *in vitro* has indicated that neurons can integrate inputs in sublinear, linear and supralinear regimes[2,3,7,8,17,18,37–39]. Synaptic inputs in these studies were activated using non-physiological stimuli under artificial conditions. How the different types of integration observed in these *in vitro* studies relate to synaptic integration *in vivo* during encoding of physiologically relevant information is unclear. Integration of binocular visual input in the visual cortex provides an ideal system for studying this issue. In mice, as in higher mammals including humans, visual inputs from the two eyes terminate in distinct and well-defined areas of the thalamus before passing on to primary visual cortex, where they converge onto single neurons[40–42]. By presenting the two eyes with independently controlled visual stimuli, it is possible to see how distinct aspects of visual information are integrated at the single-cell level. Under our experimental conditions, we found that binocular inputs were integrated either linearly or sublinearly, but not supralinearly, suggesting that active dendritic mechanisms are not recruited during binocular integration. Notably, sublinear integration of binocular inputs depended exclusively on the amplitude of the incoming monocular responses and was not related to peculiar aspects of the visual information. It therefore represents a general mode of integration in these neurons that is likely to occur under a range of stimulus conditions. The linear

and sublinear modes of dendritic integration that we observed are consistent with recent data showing that integration of visual information in layer 2/3 pyramidal neurons occurs by means of summation of distributed rather than clustered inputs[43]. In contrast, evidence exists for supralinear dendritic integration of somatosensory information in the dendrites of cortical layer 5 pyramidal[13–15] and layer 4 spiny stellate neurons[16].

Although it is well documented that the convergence of the inputs from the two eyes first happens at the level of the cortex[40–42], whether this convergence happens at the level of layer 2/3 pyramidal neurons is not known. Preprocessing of binocular input upstream of layer 2/3 pyramidal neurons could, in principle, explain the observed sublinear integration. This could occur through a decrease in excitatory input from layer 4 during strong binocular input, as a result of increased inhibition within layer 4. Alternatively, there could be an increase in inhibitory input to layer 2/3 neurons during large binocular responses, as a result of enhanced recruitment of feed-forward inhibition. Our voltage-clamp data argue against these possibilities by showing that during binocular integration both excitatory and inhibitory currents sum linearly (**Fig. 5c**,**d**). Furthermore, our voltage clamp data were well described by models using linear recruitment of excitatory and inhibitory input (**Fig. 6c**). The capacity of this 'postsynaptic' model to accurately reproduce the extent of sublinear binocular integration observed experimentally (**Fig. 6e**,**f**) strengthens the conclusion that sublinear integration is due to nonlinear interactions within layer 2/3 pyramidal neurons. Notably, this mechanism depends exclusively on the number of activated inputs and not on their origin. Indeed, our simulations showed that the extent of sublinear integration observed experimentally was independent of whether binocular inputs were integrated upstream of layer 2/3 neurons (common pool model) or arose through segregated ipsilateral and contralateral inputs (segregated model).

During binocular stimulation, we found that inhibition was recruited in a proportional manner with excitation, with an inhibitory-to-excitatory conductance ratio close to 1. Models with only excitatory synapses could not reproduce the extent of sublinear integration observed experimentally, even when we pushed these models using extreme scenarios with all excitatory inputs concentrated on the same branch or activated with high instantaneous temporal correlations. We conclude, therefore, that the recruitment of balanced inhibition is an essential component of binocular sublinear integration. Addition of inhibition makes the net reversal potential of the binocular response more hyperpolarized than with excitation alone. This increases the impact of changes in membrane potential on the driving force for current flow and thereby enhances sublinear integration. Together with other data[44,45], these findings provide further evidence that balanced recruitment of excitation and inhibition is critical for sensory processing. Moreover, our simulations show that postsynaptic sublinear integration is a robust mechanism that, in comparison to supralinear dendritic computations, is not very dependent on the precise location of incoming excitatory and inhibitory inputs.

One of the main computations thought to be performed by binocular neurons is the detection of binocular disparity, which presumably contributes to depth perception of the outside world[46,47]. Our data contribute to an understanding of how interocular phase differences are integrated at the single-cell level. Numerous single-unit (extracellular) studies in cats have explored the way that binocular neurons combine monocular inputs to encode binocular disparity[24,25,46–48]. These studies have proposed that, for most cortical cells, integration of binocular inputs can be explained by linear summation of the neuronal signals received from each eye and is strongly dependent on the phase disparity of gratings presented to the eyes. As these studies are based on action potential output, they do not provide direct information on how subthreshold synaptic inputs are integrated. By recording intracellular voltage changes from layer 2/3 pyramidal neurons during presentation of stimuli with different binocular phase disparities, we found that, at the preferred phase disparity, the underlying synaptic responses are essentially in phase and are integrated sublinearly. Importantly, sublinear integration of monocular synaptic potentials leads to linear summation of monocular firing rates during binocular stimulation (**Fig. 8f**), consistent with the linearity of binocular integration observed in earlier studies using extracellular recording[24,25,48].

At the functional level, we find that sublinear integration of binocular inputs leads to a reduction in gain of the input/output relationship. This divisive transformation has a powerful suppressive effect on the firing rate, compressing the dynamic range of neuronal output without negatively affecting the tuning properties of binocular neurons. Indeed, compared to what would happen if monocular synaptic potentials summed linearly, neurons maintained their ability to discriminate between stimulus contrast and interocular phase disparity and showed enhanced orientation selectivity (**Fig. 8i**). This latter result can be explained by considering the impact of sublinear integration on the firing output at non-preferred orientations[49]. Sublinear integration often caused the response to stimulation of both eyes at non-preferred orientations to be below action potential threshold, reducing the average firing rate at non-preferred orientations to baseline noise levels. This effect on firing rate at non-preferred orientations can explain the observed increase in the orientation selectivity index during binocular integration.

Finally, one of the key observations in our study is that inhibition is critical for sublinear integration of binocular inputs. Recent findings in mouse primary visual cortex have suggested that distinct subclasses of cortical interneurons, targeting specific neuronal compartments, are responsible for mediating different transformations of the input/output relationship of pyramidal neurons[31,49,50]. Although our simulations do not allow us to identify the location of inhibition recruited during binocular integration, the observed impact of binocular sublinear integration on orientation tuning is very similar to that found during optogenetic activation of parvalbumin-expressing interneurons[31]. This may suggest that inhibition recruited during binocular integration is largely somatic in origin. Future studies will be required to resolve the specific interneuron subtypes recruited during binocular integration and the functions of these neurons in depth perception and stereopsis.

METHODS

Methods and any associated references are available in the online version of the paper.

Note: Supplementary information is available in the online version of the paper.

ACKNOWLEDGMENTS

We are grateful to S. Solomon for discussions. We would also like to thank T. Bock for help with Matlab programming. This work was supported by the Swiss National Science Foundation, the Australian National Health and Medical Research Council and the John Curtin School of Medical Research.

AUTHOR CONTRIBUTIONS

G.J.S. and F.L. conceived the project. F.L. conducted the experiments and performed all analysis. K.I. contributed to early experiments. M.-S.T. performed all simulations. All authors discussed the data and contributed to writing the manuscript.

COMPETING FINANCIAL INTERESTS
The authors declare no competing financial interests.

1. Koch, C., Poggio, T. & Torre, V. Nonlinear interactions in a dendritic tree: localization, timing, and role in information processing. *Proc. Natl. Acad. Sci. USA* **80**, 2799–2802 (1983).
2. Larkum, M.E., Zhu, J.J. & Sakmann, B. A new cellular mechanism for coupling inputs arriving at different cortical layers. *Nature* **398**, 338–341 (1999).
3. Losonczy, A. & Magee, J.C. Integrative properties of radial oblique dendrites in hippocampal CA1 pyramidal neurons. *Neuron* **50**, 291–307 (2006).
4. Schiller, J., Major, G., Koester, H.J. & Schiller, Y. NMDA spikes in basal dendrites of cortical pyramidal neurons. *Nature* **404**, 285–289 (2000).
5. Schiller, J., Schiller, Y., Stuart, G. & Sakmann, B. Calcium action potentials restricted to distal apical dendrites of rat neocortical pyramidal neurons. *J. Physiol. (Lond.)* **505**, 605–616 (1997).
6. Stuart, G., Schiller, J. & Sakmann, B. Action potential initiation and propagation in rat neocortical pyramidal neurons. *J. Physiol. (Lond.)* **505**, 617–632 (1997).
7. Williams, S.R. & Stuart, G.J. Dependence of EPSP efficacy on synapse location in neocortical pyramidal neurons. *Science* **295**, 1907–1910 (2002).
8. Polsky, A., Mel, B.W. & Schiller, J. Computational subunits in thin dendrites of pyramidal cells. *Nat. Neurosci.* **7**, 621–627 (2004).
9. Hoffman, D.A., Magee, J.C., Colbert, C.M. & Johnston, D. K^+ channel regulation of signal propagation in dendrites of hippocampal pyramidal neurons. *Nature* **387**, 869–875 (1997).
10. Magee, J.C. & Johnston, D. Synaptic activation of voltage-gated channels in the dendrites of hippocampal pyramidal neurons. *Science* **268**, 301–304 (1995).
11. Stuart, G. & Sakmann, B. Amplification of EPSPs by axosomatic sodium channels in neocortical pyramidal neurons. *Neuron* **15**, 1065–1076 (1995).
12. Magee, J.C. Dendritic I_h normalizes temporal summation in hippocampal CA1 neurons. *Nat. Neurosci.* **2**, 508–514 (1999).
13. Murayama, M. *et al.* Dendritic encoding of sensory stimuli controlled by deep cortical interneurons. *Nature* **457**, 1137–1141 (2009).
14. Palmer, L.M. *et al.* The Cellular basis of GABAB-mediated interhemispheric inhibition. *Science* **335**, 989–993 (2012).
15. Xu, N.L. *et al.* Nonlinear dendritic integration of sensory and motor input during an active sensing task. *Nature* **492**, 247–251 (2012).
16. Lavzin, M., Rapoport, S., Polsky, A., Garion, L. & Schiller, J. Nonlinear dendritic processing determines angular tuning of barrel cortex neurons *in vivo*. *Nature* **490**, 397–401 (2012).
17. Cash, S. & Yuste, R. Input summation by cultured pyramidal neurons is linear and position-independent. *J. Neurosci.* **18**, 10–15 (1998).
18. Cash, S. & Yuste, R. Linear summation of excitatory inputs by CA1 pyramidal neurons. *Neuron* **22**, 383–394 (1999).
19. Priebe, N.J., Mechler, F., Carandini, M. & Ferster, D. The contribution of spike threshold to the dichotomy of cortical simple and complex cells. *Nat. Neurosci.* **7**, 1113–1122 (2004).
20. Chen, X., Leischner, U., Rochefort, N.L., Nelken, I. & Konnerth, A. Functional mapping of single spines in cortical neurons *in vivo*. *Nature* **475**, 501–505 (2011).
21. Varga, Z., Jia, H., Sakmann, B. & Konnerth, A. Dendritic coding of multiple sensory inputs in single cortical neurons *in vivo*. *Proc. Natl. Acad. Sci. USA* **108**, 15420–15425 (2011).
22. Kleindienst, T., Winnubst, J., Roth-Alpermann, C., Bonhoeffer, T. & Lohmann, C. Activity-dependent clustering of functional synaptic inputs on developing hippocampal dendrites. *Neuron* **72**, 1012–1024 (2011).
23. Takahashi, N. *et al.* Locally synchronized synaptic inputs. *Science* **335**, 353–356 (2012).
24. Ohzawa, I. & Freeman, R.D. The binocular organization of complex cells in the cat's visual cortex. *J. Neurophysiol.* **56**, 243–259 (1986).
25. Ohzawa, I. & Freeman, R.D. The binocular organization of simple cells in the cat's visual cortex. *J. Neurophysiol.* **56**, 221–242 (1986).
26. Jagadeesh, B., Wheat, H.S., Kontsevich, L.L., Tyler, C.W. & Ferster, D. Direction selectivity of synaptic potentials in simple cells of the cat visual cortex. *J. Neurophysiol.* **78**, 2772–2789 (1997).
27. Wang, B.S., Sarnaik, R. & Cang, J. Critical period plasticity matches binocular orientation preference in the visual cortex. *Neuron* **65**, 246–256 (2010).
28. Niell, C.M. & Stryker, M.P. Highly selective receptive fields in mouse visual cortex. *J. Neurosci.* **28**, 7520–7536 (2008).
29. Carandini, M. & Ferster, D. Membrane potential and firing rate in cat primary visual cortex. *J. Neurosci.* **20**, 470–484 (2000).
30. Tan, A.Y., Brown, B.D., Scholl, B., Mohanty, D. & Priebe, N.J. Orientation selectivity of synaptic input to neurons in mouse and cat primary visual cortex. *J. Neurosci.* **31**, 12339–12350 (2011).
31. Atallah, B.V., Bruns, W., Carandini, M. & Scanziani, M. Parvalbumin-expressing interneurons linearly transform cortical responses to visual stimuli. *Neuron* **73**, 159–170 (2012).
32. Borg-Graham, L.J., Monier, C. & Fregnac, Y. Visual input evokes transient and strong shunting inhibition in visual cortical neurons. *Nature* **393**, 369–373 (1998).
33. Cruikshank, S.J., Lewis, T.J. & Connors, B.W. Synaptic basis for intense thalamocortical activation of feedforward inhibitory cells in neocortex. *Nat. Neurosci.* **10**, 462–468 (2007).
34. Medini, P. Layer- and cell-type-specific subthreshold and suprathreshold effects of long-term monocular deprivation in rat visual cortex. *J. Neurosci.* **31**, 17134–17148 (2011).
35. Restani, L. *et al.* Functional masking of deprived eye responses by callosal input during ocular dominance plasticity. *Neuron* **64**, 707–718 (2009).
36. Williams, S.R. & Mitchell, S.J. Direct measurement of somatic voltage clamp errors in central neurons. *Nat. Neurosci.* **11**, 790–798 (2008).
37. Branco, T. & Häusser, M. Synaptic integration gradients in single cortical pyramidal cell dendrites. *Neuron* **69**, 885–892 (2011).
38. Krueppel, R., Remy, S. & Beck, H. Dendritic integration in hippocampal dentate granule cells. *Neuron* **71**, 512–528 (2011).
39. Enoki, R., Namiki, M., Kudo, Y. & Miyakawa, H. Optical monitoring of synaptic summation along the dendrites of CA1 pyramidal neurons. *Neuroscience* **113**, 1003–1014 (2002).
40. Jaubert-Miazza, L. *et al.* Structural and functional composition of the developing retinogeniculate pathway in the mouse. *Vis. Neurosci.* **22**, 661–676 (2005).
41. Muir-Robinson, G., Hwang, B.J. & Feller, M.B. Retinogeniculate axons undergo eye-specific segregation in the absence of eye-specific layers. *J. Neurosci.* **22**, 5259–5264 (2002).
42. Ziburkus, J. & Guido, W. Loss of binocular responses and reduced retinal convergence during the period of retinogeniculate axon segregation. *J. Neurophysiol.* **96**, 2775–2784 (2006).
43. Jia, H., Rochefort, N.L., Chen, X. & Konnerth, A. Dendritic organization of sensory input to cortical neurons *in vivo*. *Nature* **464**, 1307–1312 (2010).
44. Yizhar, O. *et al.* Neocortical excitation/inhibition balance in information processing and social dysfunction. *Nature* **477**, 171–178 (2011).
45. Haider, B. & McCormick, D.A. Rapid neocortical dynamics: cellular and network mechanisms. *Neuron* **62**, 171–189 (2009).
46. DeAngelis, G.C., Ohzawa, I. & Freeman, R.D. Depth is encoded in the visual cortex by a specialized receptive field structure. *Nature* **352**, 156–159 (1991).
47. Anzai, A., Ohzawa, I. & Freeman, R.D. Neural mechanisms for encoding binocular disparity: receptive field position versus phase. *J. Neurophysiol.* **82**, 874–890 (1999).
48. Ohzawa, I., DeAngelis, G.C. & Freeman, R.D. Stereoscopic depth discrimination in the visual cortex: neurons ideally suited as disparity detectors. *Science* **249**, 1037–1041 (1990).
49. Wilson, N.R., Runyan, C.A., Wang, F.L. & Sur, M. Division and subtraction by distinct cortical inhibitory networks *in vivo*. *Nature* **488**, 343–348 (2012).
50. Lee, S.H. *et al.* Activation of specific interneurons improves V1 feature selectivity and visual perception. *Nature* **488**, 379–383 (2012).

ONLINE METHODS

Animal experimentation. All the procedures were conducted in accordance with the guidelines approved by the Animal Ethics Committee of the Australian National University.

***In vivo* physiology.** Adult post-critical-period male and female C57BL/6 mice (8–10 weeks of age) were anesthetized with urethane (0.5–1 g per kilogram body weight, 10% w/v in saline, i.p.) supplemented with the sedative chlorprothixene (5 mg/kg, 10% w/v in saline, i.p.). In some cases animals were initially anesthetized with ketamine/xylazine (20 mg/kg and 3 mg/kg, i.p.) plus chlorprothixene (5 mg/kg, i.p.) and anesthesia maintained with isoflurane (0.5 to 1%). All the cells recorded under isoflurane anesthesia and included in the analysis were classified as simple cells ($n = 7$). As results obtained in these experiments were similar to those observed under urethane anesthesia, the data have been pooled. Atropine (0.3 mg/kg, 10% w/v in saline) was administered subcutaneously to reduce secretions. The level of anesthesia was assessed by loss of withdrawal reflexes in response to paw pinch. Rectal temperature was monitored and maintained at 37 ± 0.5 °C by a feedback-controlled heating blanket. The head was fixed to a custom-built head plate with cyanoacrylate glue and stabilized with dental cement. Ophthalmic lubricant gel was applied to both eyes to keep them from drying. After retracting the scalp, the area over the binocular region of the primary visual cortex was identified (2.9–3.0 mm lateral from the midline and 0.5–0.7 mm rostral to the lambda suture) and a small craniotomy (~1–2 mm in diameter) performed. To allow the insertion of recording electrodes, a hole was made in the dura using a needle and fine forcipes and the exposed cortical surface was covered with a thin layer of 0.5–1% agarose. *In vivo* whole-cell recordings were obtained using the 'blind' patch-clamp technique[51]. Electrodes were inserted into the brain at an oblique angle (30–35°) and lowered into the superficial layer of the cortex to stably record from layer 2/3 neurons in the binocular region. Subpial depths ranged from 80 to 230 µm, as estimated from the distance the micromanipulator had advanced, taking into account the angle of insertion (average subpial depth 160.1 ± 5.5 µm, $n = 81$ cells). Whole-cell current-clamp recordings were made with a current-clamp amplifier (BVC-700, Dagan Corp.) using glass pipettes (4–6 MΩ) filled with a solution containing (in mM) 130 potassium gluconate, 10 KCl, 10 HEPES, 4 Mg-ATP, 0.3 Na_2-GTP, 15 disodium phosphocreatine (pH 7.25–7.30 pH; 290–300 mOsm). Biocytin (0.2–0.5%) was added to the solution for visualization and histological identification of recorded neurons. Whole-cell voltage-clamp recordings were made with a patch-clamp amplifier (Axopatch 200B) using pipettes (3–5 MΩ) filled with the following solution (in mM): 130 cesium methansulfonate, 3 CsCl, 10 HEPES, 2 Mg-ATP, 0.3 Na_2-GTP, 10 disodium phosphocreatine, 0.3 EGTA, 1 QX-314, (pH 7.25–7.30 with CsOH; 290–300 mOsm) and biocytin (0.2–0.5%). Current and voltage signals were acquired at 50 kHz by a Macintosh computer running Axograph acquisition software (Molecular Devices) using an ITC-18 interface (Instrutech). At the end of electrophysiological recording, mice were perfused transcardially with 0.1 M PBS followed by a solution of 4% paraformaldehyde (PFA). The brain was removed from the skull and kept in PFA overnight. Coronal slices (100 µm thick) of the visual cortex were prepared and processed with the avidin–biotin peroxidase reaction (Vectastain ABC kit, Vector Laboratories). Slices were mounted in Moviol and cells reconstructed with the aid of a three-dimensional computerized system (Neurolucida, Microbrightfield Inc.; see ref. 52).

Visual stimulation. Visual stimuli were generated in Matlab using the Psychophysics Toolbox extension and consisted of sinusoidal gratings. Gratings were presented at a temporal frequency of 2 Hz, whereas the spatial frequency was optimized for each neuron within the range of 0.01–0.16 cycles/degree. Each stimulus was presented for 1.5 s (3 cycles) and preceded by a 2.5 s period of a blank screen with the same mean luminance as the stimulus. To study the dependence of binocular integration on stimulus orientation, direction and contrast, sinusoidal gratings drifting at 12 equally spaced directions (0°–330°) were displayed on a CRT monitor with gamma correction (60 Hz refresh rate, 30 cd/m^2 mean luminance) and presented in a semi-random manner to a circular patch of diameter 60° placed 25 cm in front of the mouse subtending the binocular visual space. The same stimulus was presented to each eye separately or together using computer-controlled motorized eye shutters. In experiments testing the dependence of binocular integration on interocular phase disparity mirrors were placed in front of each eye at 45° and independently controlled visual stimuli presented to separate LCD screens located on either side of the animal at a distance of 25 cm. Stimulus interocular phase disparity was varied by keeping the initial phase of the grating presented to one eye fix and by changing the initial phase of the grating presented to the other eye in 60° steps over the full range of 360°. Binocular phase disparity and stimulation condition (stimulation of the contralateral eye, ipsilateral eye or both eyes) were alternated semi-randomly. Visual stimulation were repeated three to eight times for each neuron and averaged. Gratings were displayed at 100% contrast except in experiments on the contrast-dependence of binocular integration in which stimuli were presented at three different contrasts (30, 50 and 100%).

Data analysis. *Cell classification.* Recorded cells were classified as pyramidal neurons on the basis of morphological and/or electrophysiological properties. Current-clamp experiments were performed on 65 cells. For each cell we quantified the evoked spike rate (R) in response to each grating direction (θ) as the average firing rate during the 1.5-s period of stimulus presentation minus the average spontaneous firing rate measured during the 1.5-s period before the stimulus. For each stimulation condition, the preferred direction was defined as the direction that evoked the highest spike rate (R_{pref}). In 34 cells we observed an increase in firing during presentation of the optimal stimulus to the contralateral and to the ipsilateral eye alone (**Supplementary Fig. 2g**). These cells were classified as binocular and were included in the analysis. The remaining cells either did not show visually evoked suprathreshold responses or responded exclusively to either contralateral or ipsilateral eye stimulation. We classified binocular neurons as simple or complex cells on the basis of their firing in response to drifting gratings at the preferred orientation presented to the contralateral eye as reported previously[19,53] (**Supplementary Fig. 2a**,**b**).

Voltage-clamp experiments were performed on 16 cells. The neuron's preferred direction was estimated as the one that evoked the largest excitatory postsynaptic current (EPSC) when holding the cell at −80 mV (refs. 30,31). In 12 cells we measured a visually evoked EPSC during presentation of the optimal stimulus to the contralateral (average EPSC peak amplitude = −159.2 ± 35.3 pA) as well as the ipsilateral eye (average EPSC peak amplitude = −109.8 ± 24.9 pA). These cells were classified as binocular and were included in the analysis.

Tuning properties. Evoked spike rates across all stimulus directions were used to determine the orientation tuning properties of the neuron during stimulation of the contralateral or ipsilateral eye alone (**Supplementary Fig. 2**) and for the simultaneous stimulation of both eyes together (**Fig. 8**). The neuron's preferred orientation, direction selectivity index (DSI), orientation tuning width (half-width at half height, HWHH) and ocular dominance index (ODI) were determined as reported previously[27,28]. The orientation selectivity index (OSI) was computed as 1 − circular variance (refs. 30,54). A neuron that responds exclusively to a single orientation will have an OSI = 1, whereas neurons that respond equally to all orientations will have an OSI = 0. Calculation of the OSI based on the spike rate at the preferred and orthogonal (R_{orth}) directions using $(R_{pref} - R_{orth})/(R_{pref} + R_{orth})$ (ref. 28) gave similar results. Matching of the preferred orientation across stimulation conditions was computed as 1 − circular variance, with the circular variance being calculated on the preferred orientation determined separately during stimulation of each eye alone and for stimulation of both eyes together. Values close to 1 indicate perfect matching.

Synaptic responses. To study how binocular neurons integrate synaptic inputs from the contralateral and ipsilateral eye, voltage traces recorded in current-clamp were processed to obtain an estimate of the overall synaptic response that underlies action potential generation. This was achieved by applying a sliding median filter of 10 ms width to all raw traces to selectively remove action potentials while preserving the overall subthreshold membrane potential dynamics (**Supplementary Fig. 1a**–**c**). Median-filtered traces were then averaged over a single stimulus cycle (0.5 s) and across stimulus repetitions[29]. We then fitted the average single cycle response with a 2-Hz sinusoidal function from which we measured the following parameters: the mean component (V_{mean}), quantified as the average potential over the stimulus presentation period relative to a 1.5-s baseline period before the stimulus; the modulation component ($V_{modulation}$), defined as the amplitude of the fitted sinusoid; and the peak response (V_{peak}), defined as the sum of the mean and modulation components. Analysis performed on supra- and subthreshold responses to visual stimulation revealed a negligible impact of median filtering on the quantification of V_{mean}, $V_{modulation}$ and V_{peak} (**Supplementary Fig. 1d**–**h**).

Binocular integration. To investigate how the different components of synaptic responses summate during binocular stimulation, we compared the observed response when the two eyes are stimulated together to the linear sum of the responses to stimulation of each eye separately. Residuals from linearity are calculated as the difference between the observed response during binocular stimulation and the expected linear sum of responses to stimulation of each eye alone. To measure the linearity and residuals from linearity as a continuous function over the period of stimulation, traces were binned in 10-ms epochs and a point-by-point analysis performed for each time bin.

Synaptic current and conductance estimates. Currents evoked by the presentation of sinusoidal gratings were recorded during somatic whole-cell voltage-clamp without compensation for series resistance at two holding potentials. Neurons were voltage-clamped at the predicted reversal potential for inhibition (−80 mV, $n = 12$ cells) to record EPSCs, and close to the reversal potential for excitation (average: 25.5 ± 1.6 mV, $n = 10$ cells) to record inhibitory postsynaptic currents (IPSCs). Series resistance assessed from the amplitude of the capacitance transient at the onset of a voltage step was on average 35.1 ± 2.8 MΩ ($n = 12$ cells). Excitatory and inhibitory conductances were estimated as previously described[32,33], after correction for the junction potential (~10 mV) and series resistance and assuming reversal potentials for excitation and inhibition of 0 mV and −80 mV, respectively.

Nonlinear threshold model. The relationship between the membrane potential and spike rate (R) was described with the following two-parameter model[19]:

$$R(V_m) = k \times [(V_m - V_{rest})_+]^p$$

where V_m is the membrane potential during the stimulus presentation and V_{rest} is the resting membrane potential during baseline conditions; k and p are free parameters, corresponding to a gain factor and a power-law exponent, respectively, and were determined based on least-square fitting. The subscript "+" indicates rectification (membrane potential values below zero were set to zero). The fitted parameters were used to predict the firing rate associated with linear integration of binocular synaptic inputs.

Neuron model. Computer simulations were performed using the NEURON simulation environment on a Linux desktop computer running Ubuntu 12.04 LTS. A multicompartment model was obtained by reconstructing a biocytin-filled layer 2/3 pyramidal neuron. The reconstructed neuronal model consisted of 136 compartments, subdivided into a total of 1,021 segments. All dendritic branch diameters were scaled by a factor of 1.3 to account for cell shrinkage. Specific membrane resistance (R_m), capacitance (C_m; 1 μF/cm^2) and internal resistance (100 Ω/cm) were uniformly distributed throughout the model. In current clamp simulations the resting membrane potential was set to −70 mV and R_m to 8,000 Ω/cm^2, giving an apparent membrane time constant (8 ms) and input resistance (80 MΩ) similar to those observed for this cell at the resting membrane potential *in vivo*. In voltage-clamp simulations the resting membrane potential was set to −52 mV to match holding currents recorded at hyperpolarized and depolarized potentials in these experiments. Spines were incorporated into the model by decreasing R_m and increasing C_m by a factor of 2 in distal dendritic compartments (>40 μm from the soma). No voltage-gated ion channels were included in the model. The series resistance of the somatic voltage-clamp 'electrode' in voltage-clamp simulations was set to 35 MΩ to match the average series resistance in experimental voltage-clamp recordings.

In models with dendritic inhibition 1,000 excitatory and 300 inhibitory synapses were distributed randomly throughout the basal dendrites, with the density of inputs on a selected segment proportional to its surface area. Models with somatic inhibition contained 800 excitatory synapses distributed throughout the basal dendrites plus 180 inhibitory synapses at the soma. Excitatory inputs representing contralateral and ipsilateral inputs were sampled from the same pool (common pool model) or segregated into two pools with 60% classified as contralateral and 40% classified as ipsilateral (segregated model). As seen in the Results, there was essentially no difference between common pool and segregated models. The conductance change at excitatory synapses had an exponential rise and decay of 0.2 and 2 ms, respectively, a peak of 150 pS and a reversal potential of 0 mV. Using these parameters, the average unitary EPSP amplitude at the soma during activation of inputs randomly distributed throughout basal dendrites was 0.164 ± 0.018 mV, consistent with previous experimental findings[55]. The conductance change at inhibitory synapses had an exponential rise and decay of 0.2 and 10 ms, respectively, a peak of 150 pS and a reversal potential of −80 mV. In simulations with current-based synapses, 'excitatory' inputs had an amplitude of −2.8 pA, whereas 'inhibitory' inputs had an amplitude of +1.1 pA in the models with dendritic inhibition and +0.7 pA in models with somatic inhibition, with only excitatory inputs activated at hyperpolarized potentials and only inhibitory inputs activated at depolarized potentials. To simulate the response to drifting gratings, synapses were activated in a sinusoidal manner (2 Hz modulation) by independent, nonhomogeneous Poisson processes to match experimentally recorded currents and voltages during visual input. In the common pool model, excitatory inputs were activated at rates between 0.54 (trough) and 27.54 Hz (peak) during contralateral input, between 0.36 and 18.36 Hz during ipsilateral input, and between 0.9 and 45.9 Hz during binocular input. In the segregated pool model, the different sets of contralateral and ipsilateral synapses were activated at rates between 0.9 and 45.9 Hz. The effective probability of release was 1.

In models with only excitatory input (**Fig. 7**), synapses were distributed on basal dendrites in different spatial configurations. In the dispersed configuration, contralateral and ipsilateral inputs were randomly distributed onto all dendritic branches. In the partitioned configuration, contralateral and ipsilateral inputs were distributed onto different dendritic branches such that no single branch contained both inputs. In the clustered configuration, all contralateral and ipsilateral inputs were positioned on the same, single dendritic branch. The number of synapses in the different models was 500 (dispersed), 550 (partitioned) and 700 (concentrated), and their activation was varied at rates between 1 Hz (trough) and 80 Hz (peak). Temporal correlations between synaptic inputs were introduced by using a common Poisson input train to drive sets of 50 synapses. This was the highest temporal correlation possible while still maintaining modulated responses similar to those seen experimentally. Common input trains were either restricted to within the contralateral and ipsilateral pools (monocular correlation) or shared between the pools (binocular correlation). In these simulations, the number and distribution of excitatory synapses was identical to that in the dispersed configuration.

Statistics. Statistical analysis used Prism 4.0 for Macintosh (GraphPad Software, Inc.). Average values are given as mean ± s.e.m. Statistical comparison between two sets of matched data used a two-tailed paired t-test. When comparing three or more sets of data, we used either a one-way or two-way ANOVA followed by a Bonferroni *post hoc* multiple comparison test. A chi-squared test was used when comparing sets of data with categorical outcome as the variable, and the Pearson's correlation coefficient was used when testing for significant correlations between two variables. All data sets were tested for normality. Significance was set at $P < 0.05$.

51. Margrie, T.W., Brecht, M. & Sakmann, B. *In vivo*, low-resistance, whole-cell recordings from neurons in the anaesthetized and awake mammalian brain. *Pflugers Arch.* **444**, 491–498 (2002).
52. Kole, M.H., Brauer, A.U. & Stuart, G.J. Inherited cortical HCN1 channel loss amplifies dendritic calcium electrogenesis and burst firing in a rat absence epilepsy model. *J. Physiol. (Lond.)* **578**, 507–525 (2007).
53. Skottun, B.C. *et al.* Classifying simple and complex cells on the basis of response modulation. *Vision Res.* **31**, 1079–1086 (1991).
54. Ringach, D.L., Shapley, R.M. & Hawken, M.J. Orientation selectivity in macaque V1: diversity and laminar dependence. *J. Neurosci.* **22**, 5639–5651 (2002).
55. Silver, R.A., Lubke, J., Sakmann, B. & Feldmeyer, D. High-probability uniquantal transmission at excitatory synapses in barrel cortex. *Science* **302**, 1981–1984 (2003).

doi:10.1038/nn.3394